International Journal of Heat and Mass Transfer 51 (2008) 5247–5259

Contents lists available at ScienceDirect

International Journal of Heat and Mass Transfer

journal homepage: www.elsevier.com/locate/ijhmt

Endwall heat transfer and pressure drop in rectangular channels with attached and detached circular pin-fin array

S.W. Chang [a,*], T.L. Yang [a], C.C. Huang [a], K.F. Chiang [b]

[a] Thermal Fluids Laboratory, Department of Marine Engineering, National Kaohsiung Marine University, No. 142, Haijhuan Road, Nanzih District, Kaohsiung 811, Taiwan, ROC
[b] Thermal Dissipation Department, AVC International Company, Taiwan, ROC

ARTICLE INFO

Article history:
Received 21 August 2007
Received in revised form 28 February 2008
Available online 5 May 2008

Keywords:
Detached pin-fins
Heat transfer enhancement
Pressure drop

ABSTRACT

Endwall heat transfer and pressure drop characteristics in four rectangular channels with a channel aspect ratio of 4 and the staggered arrays of circular pin-fins with four clearances (C) between pin-tips and the measured endwall of 0, 1/4, 1/2 and 3/4 pin-diameter (d) are examined comparatively at Reynolds numbers (Re) of 10,000, 15,000, 20,000, 25,000 and 30,000 to determine the effects of pin-tip leakages on the endwall heat transfer and on channel inlet-to-exit pressure drops. The accelerated flows through pin-to-endwall clearances modify the protrusion-endwall interactions that affect the horseshoe vortices as well as the downstream wakes and shear layer separations. By way of increasing C/d ratio from 0 to 3/4, the area averaged endwall Nusselt numbers decrease with substantial reductions in channel inlet-to-exit pressure drops. The endwall heat transfer level with detached pin-fins at $C/d = 1/4$ is somewhat less than that with attached pin-fins but the pressure drop coefficient of the former is much lower than that of the later, which leads to the highest thermal performance factor among the four comparative cases in the Re range examined by this study. A set of correlations that evaluate the area averaged endwall Nusselt number and the pressure drop coefficient with Re and C/d as the controlling parameters are derived.

1. Introduction

Pin-fin channel appears as an effective heat transfer enhancement (HTE) method but with high pressure drop penalties that evolves from the early studies of heat transfer over tube bundles with cross flows for shell-and-tube heat exchangers. As a HTE measure, historical developments of studies for pin-fin channels [1–27] divert the research focus toward the endwall heat transfer performances in addition to those on the pins. The different flow physics in association with the heat transfer performances over the surfaces of pins and endwalls result in the higher heat transfer levels on pin surfaces by 35% [4] or 10–20% [18] over those on endwalls. Based on the results for tube bundles with cross flows, it is well known that the fluid mixing and unsteadiness from the wakes tripped by individual rows of tubes increase progressively as the flow traverses further downstream through the tube bank. Heat transfer performances over the first 3–4 tube-rows therefore increase progressively with the three dimensional advection and turbulence diffusion enhanced in the further downstream. This causes the primary and secondary horseshoe vortices near the protrusion-endwall junctions to be more diffuse and the endwall reattachments due to separated shear layers behind the pins to be less distinct and separate at the developed flow region. As a result, heat transfer rates on the surfaces of endwalls and pin-fins increase streamwisely over the first few rows of pin-fin array even if the downstream boundary layers grow thicker. Local endwall heat transfer distributions show less distinct features in the developed flow region relative to its developing counterpart in a pin-fin channel [21].

In either the developing or developed flow region of a pin-fin channel, the protrusion-endwall configurations as well as the pin-fins trigger a number of complex vortex structures that affects the endwall heat transfer performances. Of the primary importance for endwall HTE performances is the horseshoe vortices that form upstream of each pin at pin-endwall junction. Regional HTE effects are generated by the secondary advection of horseshoe vortices as they advect away from the stagnation line on the upstream edge of each pin that rolls the cooler fluids toward the heated endwall [15]. Two legs of each horseshoe vortex, rolling around the adjoining pin, advect further downstream to form near the edges of the pin-fin wake [21]. But the wake behind each pin recirculates the heated coolant and generates a low heat transfer region behind the pin. Further downstream of the re-circulation zone with low flow velocities, the reattachment due to shear layer separation elevates local heat transfer again. Along the edges of these wakes, the separated shear layers promote turbulence productions and transportations which lead to two concentrated high heat transfer

* Corresponding author. Tel.: +886 7 612 6256; fax: +886 7 362 9500.
E-mail address: swchang@mail.nkmu.edu.tw (S.W. Chang).

0017-9310/$ - see front matter © 2008 Elsevier Ltd. All rights reserved.
doi:10.1016/j.ijheatmasstransfer.2008.02.046

Nomenclature

English symbols

A, B, m, n	coefficients in correlations
C	clearance between pin-tip and endwall (m)
D	hydraulic diameter of channel (m)
d	diameter of each circular pin-fin (m)
f	fanning friction factor = $[\Delta P/(0.5\rho W_m^2)]/(D/4L)$
f_∞	fanning friction factor of Blasius equation = $0.079\,Re^{-0.25}$
H	channel height (m)
k_f	thermal conductivity of fluid (W m^{-1} K^{-1})
L	channel length (m)
Nu	local endwall Nusselt number = $qD/k_f(T_w - T_b)$
$\overline{Nu}$	endwall area-averaged Nusselt number
Nu_∞	Nusselt number value for developed flow in smooth-walled plain tube
P_x	X-wise pitch of pin-fin array (m)
P_y	Y-wise pitch of pin-fin array (m)
ΔP	pressure difference between two pressure taps (N m^{-2})
q	convective heat flux (W m^{-2})
Re	Reynolds number = $\rho W_m D/\mu$
T_b	fluid bulk temperature (K)
T_w	local wall temperature (K)
W	channel width (m)
W_m	mean flow velocity (m s^{-1})
X	axial location referred to flow entry as origin (m)
Y	spanwise location referred to bottom edge of flow entry as origin (m)

Greek symbols

ρ	density of fluid (kg m^{-3})
μ	fluid dynamic viscosity (kg m^{-1} s^{-1})
η	thermal performance factor = $(\overline{Nu}/Nu_\infty)/(f/f_\infty)^{1/3}$

Superscripts

A	attached pin-fins
D	detached pin-fins

regions aside each pin. Although these flow features characterize the flow physics in a pin-fin channel that generalize the endwall heat transfer performances, the HTE effectiveness and pressure drop characteristics also vary with by-pass flows over pin-tips [1,20,24], height-to-diameter ratios of pins [3–5,8], shapes [6,11,15,17,19,20,24–26], arrangements [2,7,10,12–14,18,19,22–24], materials [14] and the three-dimensionality [8,9,13,15,16] of pins as well as the orientation of pin-array in the cross flow [6,27]. Theses geometric factors are sometime interrelated to affect the endwall heat transfer performances and the pressure drops of pin-fin channels. In light of endwall heat transfer performances, the systematic reduction of inclined angles of pin-fins mounted on endwalls from 90° to 40° in a narrow rectangular channel incurs the consistent decreases of averaged endwall heat transfer levels and pressure drops [27]. Averaged endwall heat transfer rates for relatively short pins are slightly lower than for long pins but the pressure drops display no such differences [7]. The staggered diamond pin-fin array with pitch ratios of 1.5–2.5d offers the considerable HTE effects; while the elliptical pins provide the higher thermal performance factors when the HTE ratio is rationalized by the augmented pressure loss [26]. These studies [1–26] always assure that the increase in endwall heat transfer is accompanied by a substantial increase in pressure losses. Nevertheless, with the performance analysis of rectangular ducts enhanced by the staggered square pin-fins [20], the increase of pin-tip clearance from the untouched endwall systematically reduces the endwall heat transfer level and the pressure drop coefficient. When the C/d ratios vary in the range of 1–8, the pin-tip leakage effects on overall thermal resistance of the pin-fin array appear to be minor but the considerable reductions in pressure drops through such pin-fin sinks are observed at the pin-pitch of 2.2d [24]. Although it has been a long term fact that the pin-tip by-pass flows can considerably reduce the pressure drops through pin-fin channels, the accompanying moderation of their HTE effectiveness has prohibited the further progress to explore the thermal performances of detached pin-fins with very small pin-tip clearances from the untouched endwall. No previous work has been reported on the endwall heat transfer and pressure drop in a pin-fin channel with the C/d ratio less than 1. Inspired by the experiences gained from the detached ribs [28] for heat transfer elevations, the very small C/d ratios can result in the local wall-flow accelerations and trip the additional separated shear layers for promoting local heat transfer on the endwall. As a preliminary study for pin-fin channels with detached pin-fin arrays, this study compares the detailed endwall heat transfer distributions at C/d = 0, 1/4, 1/2 and 3/4 as Re = 10,000, 15,000, 20,000, 25,000 and 30,000 with the pressure drop characteristics examined. It is worth noting that the detached pin-fins offer the additional convective cooling areas on pin-tips and over the untouched endwall. Thermal performance factors based on constant pumping power consumptions are compared for four rectangular channels with a set of identical pin-array configurations but different C/d ratios.

2. Experimental details

The detailed endwall heat transfer measurements are performed using the steady-state method with wall temperature profiles detected from the infrared radiometer. The flow circuit with measurement devices, data acquisition systems, heat loss and heat transfer experiments and the method of data processing follow our previous work reported in [29]. References to evaluate the HTE effectiveness and the pressure drop augmentation for four tested pin-fin channels are respectively evaluated from the Dittus–Boelter correlation as Nu_∞ [30] and the Blasius equation as f_∞. Thermal performance factors (η) are accordingly quantified as $(\overline{Nu}/Nu_\infty)/(f/f_\infty)^{1/3}$ where $\overline{Nu}$ and f are the endwall area-averaged Nusselt number and the Fanning friction factor based on the inlet-to-exit pressure drop of each pin-fin test channel.

2.1. Experimental apparatus

Fig. 1 depicts the constructional details of the test module for heat transfer and pressure drop measurements. The origin of present X–Y coordinates specifies at the bottom left corner of the scanned endwall as indicated in Fig. 1. Fourteen staggered rows of circular pin-fins (1) with the X-wise and Y-wise pin-pitches of 2d are mounted on the Teflon back endwall (2) normal to the coolant flow inside the rectangular test section (3). The ratio of channel width (80 mm) to channel height (20 mm) referring to as the channel aspect ratio is 4 which gives the hydraulic diameter (D) of 32 mm. These pins are made of the thermally insulating material (Teflon) with a diameter (d) of 8 mm so that the additional fin effects for HTE effectiveness are absent. Endwall heat transfer and pressure drop measurements are performed for the rectangular channel fitted with four sets of pin-fin arrays with different pin-heights those produce the clearances (C) of 0, 1/4, 2/4 and 3/4d between pin-tips and the heated endwall (4). The heating surface

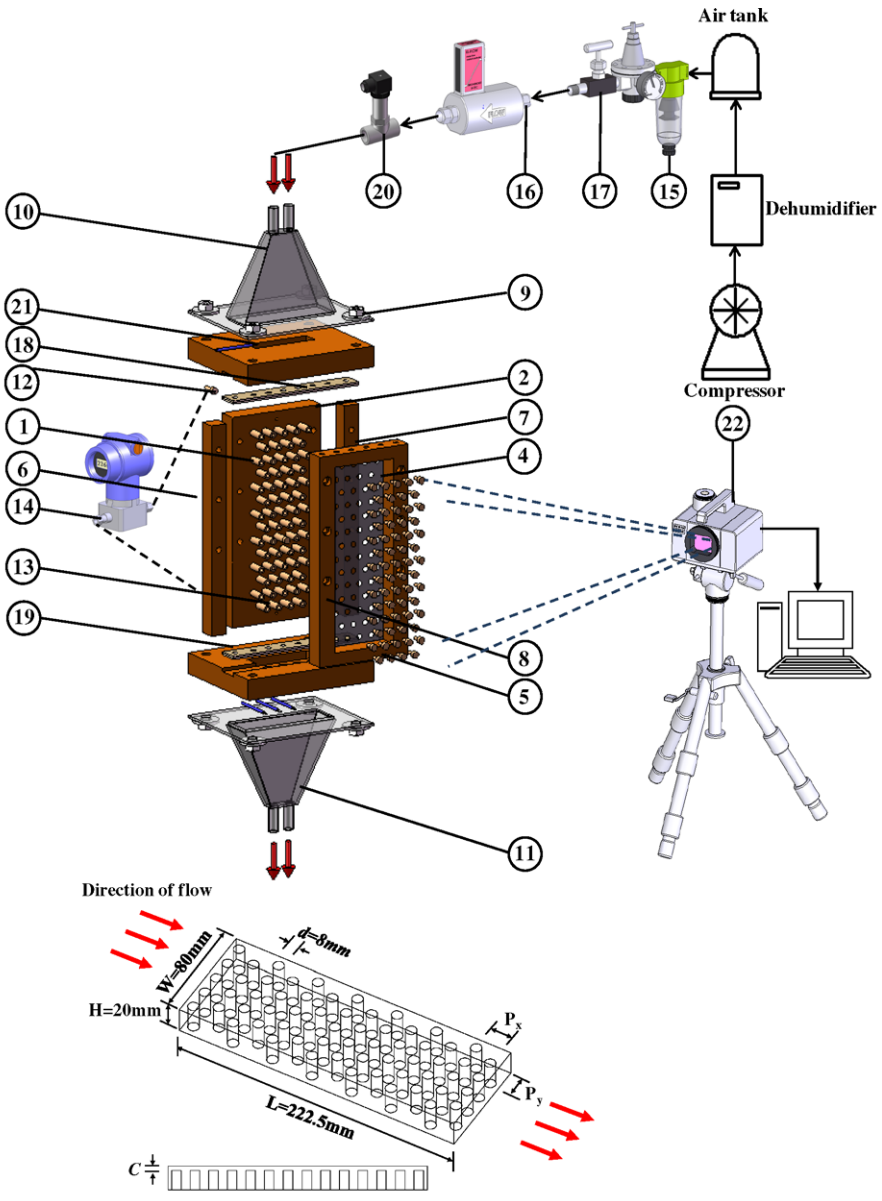

W (channel width) = 80mm H (channel height) = 20mm L (channel length) = 270mm
d (pin diameter) = 8mm P_x (X-wise pin pitch) = 16mm P_y (Y-wise pin pitch) =16mm
C (pin-tip clearance) = 0, 2mm, 4mm, 6mm H (pin height) = 20mm

Channel aspect ratio (W/H) = 4
Pin-array Y-wise pitch ratio (Py /*d*) = 2
Pin height -to-diameter ratio (H/d) = 2.5
Pin-array X-wise pitch ratio (Px /*d*) = 2
Pin-tip clearance ratio (*C*/*d*) = 0, 1/4, 2/4, 3/4

(1) Teflon pin-fins (2) Teflon back endwall (3) test section
(4) heating foil (5) Teflon end-cover pin (6)(7) Teflon sidewalls
(8) Teflon frame (9) draw bolts (10)(11) entry/exit plenum chambers
(12)(13) entry/exit pressure taps (14) micro manometer
(15) filtering unit (16) mass flow meter (17) needle valve
(18)(19) entry/exit copper plates (20) pressure transducer
(21) thermocouple (22) infrared radiometer

Fig. 1. Experimental apparatus.

(4) over which the wall temperatures (T_w) are scanned is made of a continuous 80 mm wide, 222.5 mm long and 0.1 mm thick stainless steel foil. With the attached pin-fin array ($C = 0$), each pin is tightly jointed with the heated endwall (4) by penetrating a Teflon end-cover pin (5) through the heating foil (4) into each Teflon pin (1) of the array. Adjustable DC electrical powers are directly fed

through the heating foil (4) that simulates the basically uniform heat fluxes thermal boundary over the endwall. The scanned heating foil (4) is sandwiched between two Teflon sidewalls (6)(7) and one Teflon frame (8). The complete set of test section is tightened by four draw bolts (9) between the entry (10) and exit (11) plenum chambers. The convergent entry plenum chamber (10) joins with the pin-fin channel (3) to simulate the abrupt entry condition. Prior to the heat transfer test section (3), honeycombs and steel meshes are installed inside the entry plenum chamber (10). Through the back wall (2) of the pin-fin channel, two pressure taps (12)(13) are fitted at the locations adjoining the entry and exit planes of the test section through which the entry-to-exit pressure drops are measured by the digital micromanometer (14). Prior to entering the entry plenum chamber, the dehumidified and cooled airflow from the air tank is channeled through a set of pressure regulator and filtering unit (15), a mass flow meter (16) and a needle valve (17) where the mass flow rate is detected and adjusted. Two ends of the heating foils (4) are sandwiched between the insulation Teflon plates and the entry and exit copper plates (18)(19) those connect with copper bars to complete the electrical heating circuit. In order to control the prescribed *Re* at the entry plane of the test section within ±1% discrepancy from the targeting value, the coolant mass flow rate specified by the tested *Re* is frequently adjusted to compensate the property variations of the test fluid due to temperature variations as a result of heat transfer. This requires the pressures and temperatures of test coolant in the entry plenum chamber (10) to be metered by a set of pressure transducer (20) and type K thermocouple (21). The evaluation of local fluid bulk temperature (T_b) is based on the enthalpy balance method. The convective heat flux (q) at a selected X location is obtained by averaging all the spanwise q data collected at the X location as $q(X)$. Having determined $q(X)$ and the through flow mass flow rate ($\dot{m}$), the T_b increase between two successive measurement locations in X direction is determined as $\Delta T_b = q(X) \times$ heating area$/(\dot{m}C_p)$ where C_p is the specific heat of coolant evaluated at the constant pressure. The T_b value at each detected X location is obtained following such successive calculation procedure starting from the T_b measurement at flow entry. Three additional type K thermocouples are equally spaced along the spanwise centerline over the exit plane of the test section to measure the flow exit temperatures in order to check the accuracy of T_b evaluation. Detailed T_w measurements over the scanned endwall are imaged by a calibrated two dimensional infrared radiometer (22). The reference fluid temperature is defined as the local fluid bulk temperature to evaluate the local Nusselt number and the fluid properties such as the thermal conductivity and viscosity. Characteristic length selected to define *Re* and *Nu* is the hydraulic diameter of test channel (D).

2.2. Program and data processing

With five tested *Re* of 10,000, 15,000, 20,000, 25,000, 30,000 and four C/d ratios of 0, 1/4, 2/4, 3/4, 1, the heat transfer coefficients are measured at the steady states, while the entry-to-exit pressure drops are individually measured at isothermal conditions. With heat transfer tests, heater powers are constantly adjusted to control the hottest spot over the heated endwall at 373 K. Having adjusted the heater power or the airflow rate, the corresponding steady state is assumed when the variations of wall temperatures between several successive scans are less than 0.3 °C. Transition periods for steady states generally take 45 min after the adjustment of heating power or airflow rate. The on-line data acquisition system is activated as the steady state condition is satisfied that records all the T_w measurements as well as the relevant measurements such as the heater power, the mass airflow rate and T_b measurements for the subsequent data analysis. These raw measurements are converted into local *Nu* over the scanned endwall using Eq. (1)

$$Nu = qD/k_f(T_w - T_b) \tag{1}$$

The local convective heat flux (q) in Eq. (1) is obtained by subtracting the local heat loss flux from the total heat flux supplied. The characteristics of external heat loss at various temperature levels were determined from a number of heat loss calibration runs. Each set of calibration test runs was performed with the flow blocked off with the fiberglass thermal insulating material filled in the channel. The heat supplied to the heating foil was entirely lost externally. The supplied heating power was balanced with the external heat loss at the corresponding steady-state temperature distributions. A review of wall temperature data collected from the entire heat loss calibration runs showed the less than 2.56% of non-uniformity in the wall temperature distributions. The plot of heat loss flux against the corresponding steady wall-to-ambient temperature difference revealed a linear-like functional relationship, which correlated the heat loss flux with the local wall-to-ambient temperature difference. As the pin-fin array generates spatial heat transfer variations, the local wall temperatures varied spatially during heat transfer tests. Therefore the external heat loss remained as a spatial function that resulted in the non-perfect uniform flux heating condition over the endwall. With the attached pin-fins, the endwall heating area used to evaluate the heat flux excludes the contacting area of pins. With detached pin-fins, the endwall heating area is obtained by multiplying the channel-height with channel-length for evaluating the heat flux. The ratio of endwall convective areas between the detached and attached pin-fins is 1.216 for the present test section. Heat loss fluxes increase as wall-to-ambient temperature differences increase. The proportionality between the heat loss flux and the wall-to-ambient temperature difference is determined through a series of calibrating tests for each test module. Such heat loss proportionality is combined into the data processing program to account the distributions of endwall heat loss flux. As the local heat loss fluxes vary with T_w distributions, the distributions of convective heat flux are accordingly affected by the endwall T_w distributions. However, as the maximum proportion of heat loss flux for the present series of tests is about 9.3%; the endwall thermal boundary is controlled at the basically uniform heat flux condition. Having determined the profiles of convective heat flux over the endwall, the local fluid bulk temperature (T_b) is sequentially evaluated using the enthalpy balance method starting from the T_b measurement at the entry plane of the test section. The calculated T_b value is constantly checked with the averaged T_b measurements at the exit plane of test section. Data batches can only be recorded when the differences between the calculated and measured T_b values are less than 10%. Fluid properties required to define *Re*, *f*, and *Nu* are accordingly evaluated from the local fluid bulk temperature. With pressure drop tests, the dimensionless pressure drop coefficients are evaluated as the Fanning friction factors (f) using the pressure drops (ΔP) across the pin-fin test section of length L with mean flow velocity (W_m) as

$$f = \Delta P/(0.5\rho W_m^2)(D/4L) \tag{2}$$

A set of correlations that evaluate the area averaged endwall Nusselt number ($\overline{Nu}$) and the pressure drop coefficient (f) with *Re* and C/d ratio as the determined variables are derived. Thermal performance factors (η) are subsequently analyzed to compare the overall thermal performances of four tested pin-fin channels with C/d ratios of 0, 1/4, 2/4, 3/4 and 1.

The maximum uncertainties of *Nu*, *f* and *Re* are calculated in accordance with the policy of ASME J. Heat Transfer on reporting the uncertainties in experimental measurements and results [31]. The major sources for attributing experimental uncertainties of

Nu and *f* originate from the temperature and pressure drop measurements respectively. Our previous repeatability calibration tests for the present infrared thermal image system indicated the maximum uncertainty of temperature measurements is ±0.7 K The precision of the present micromanometer is 0.01 mmH_2O. With wall-to-fluid temperature differences and pressure drops respectively fall in the ranges of 299.6–301.3 K and 10.3–233.6 mmH_2O, the maximum uncertainties associated with *Nu*, *f* and *Re* are estimated as 10.2%, 4.8% and 2.1% respectively.

3. Results and discussion

3.1. Detailed endwall **Nu** distributions

Fig. 2 illustrates the effects of *C*/*d* ratio on endwall heat transfer by comparing the *Nu* distributions over four endwalls with (a) attached pin-fins and detached pin-fins of (b) *C*/*d* = 1/4, (c) *C*/*d* = 2/4, (d) *C*/*d* = 3/4 at *Re* = 30,000. The typical endwall *Nu* distributions for the channel with attached pin-fins are shown in Fig. 2a where the effects of wake shading and turbulent mixing of the mainstream flow result in the evidently high *Nu* regions at the leading and trailing edges of each pin. The horseshoe vortices are formed upstream of each pin at the pin-wall junction that convect downstream away from the stagnation line. Two legs of these vortices advect around each adjoining pin that roll the cooler fluids toward the heated endwall. Trajectories of these primary and secondary vortices on the endwall show the higher heat transfer regions around and behind each pin-fin (see Fig. 2a). In front of each pin, the downstream wakes tripped by its upstream pins interact with the vortical flows with high velocity and high vorticity to produce the large scale unsteadiness over the shear layers that results in a rim of high *Nu* region right on the leading edge

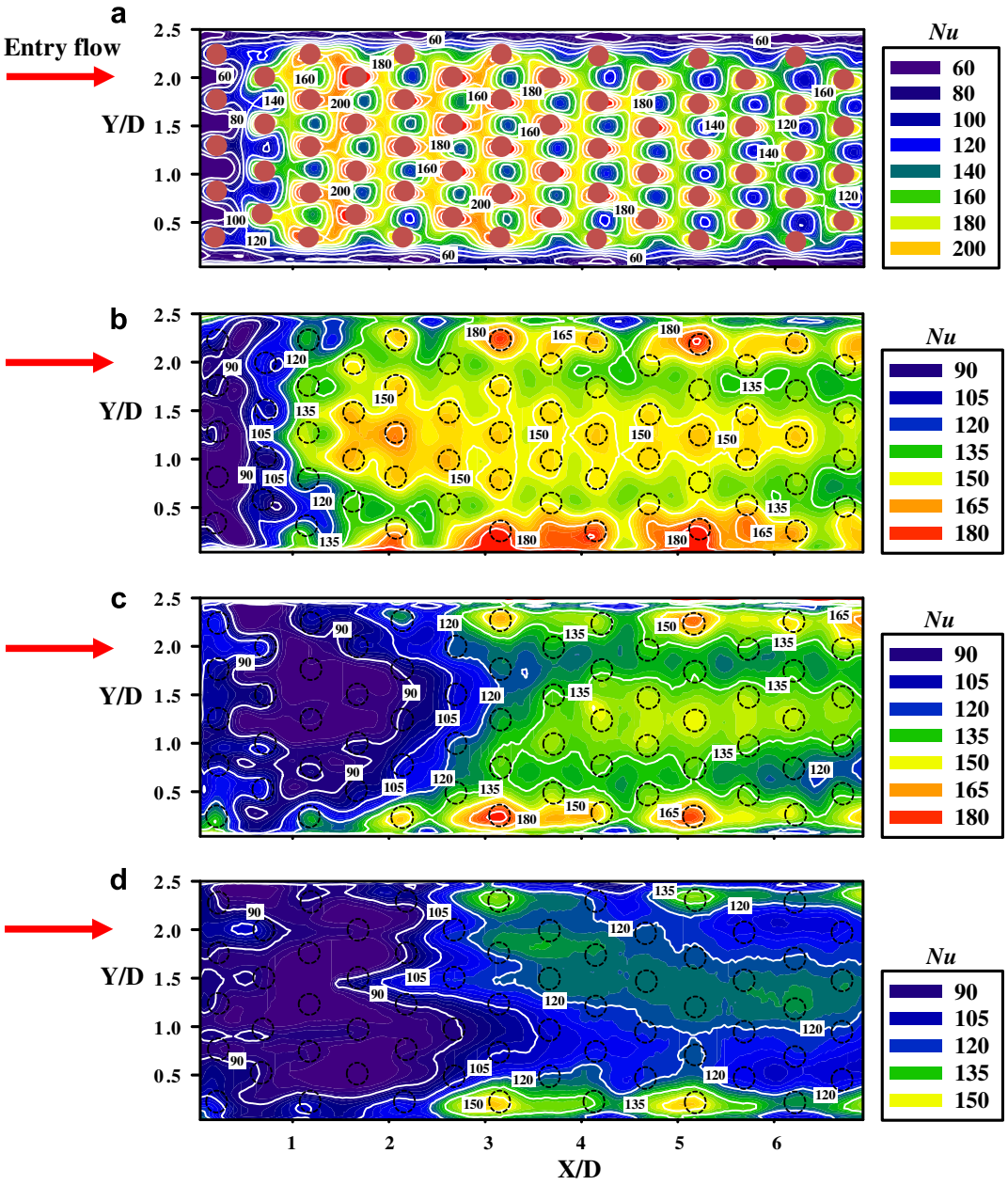

Fig. 2. Endwall *Nu* distributions for test channels with (a) attached pin-fins (b) detached pin-fins of *C*/*d* = 1/4, (c) detached pin-fins of *C*/*d* = 2/4 and (d) detached pin-fins of *C*/*d* = 3/4 at *Re* = 30,000.

of each pin [32]. But the relatively low *Nu* values develop between two adjacent pins in each pin-row and over the outer edges of the pin-array along two sidewalls. Areas with low *Nu* values between two adjacent pins in each pin-row are in the wake regions downstream of the pins that agree favorably with those observed by Won et al. [21] due to the relatively low flow velocities; while the low *Nu* stripes along two sidewalls of the pin-fin channel reflect the typical boundary layer flow behaviors with almost vanished HTE effects. In the case of $C/d = 0$, the flow measurements clearly indicate that the presence of cylindrical pin-fins suppresses the corner structures most likely due to the increased mixing via the mainstream interactions with pin-fins [33]. Such suppressed corner vortices adjacent to both sidewalls serve the physical rationale for low *Nu* bands along two sidewalls. Above all, these heat transfer signatures described by Fig. 2a are the primary results of the vortex pair that is generated by the blockage and streamline displacement effects of pin-fins, as well as the advection of two legs of horseshoe vortices. Also evidently shown in Fig. 2a are the results of two competing flow mechanisms, namely the streamwise increase of turbulent mixing due to wake shading from the upstream pin-rows and the thickened boundary layers downstream. The streamwise increases of heat transfer levels from the entrance to the third pin-row as shown in Fig. 2a indicate that the effect of enhanced turbulent mixing and HTE effectiveness due to vortex shading has overcome the suppressed HTE effect due to the thickened boundary layers. In the regions between the third and fifth pin-rows where the thermal flow field is not fully developed, the higher heat transfer rates along with the distinct heat transfer signatures due to the complex vortices and secondary flows tripped by pin-fins and the pin-wall junctions are observed (see Fig. 2a). At locations further downstream toward the developed flow region, the typical endwall *Nu* distributing patterns observed in the region between pin-rows 3–5 are still followed but the degrees of heat transfer elevation are reduced with relatively vague spatial *Nu* variations. Here, the boundary layers over the endwall are getting thicker and the three-dimensionality of wake shading and turbulent mixing is enhanced that causes the vortices to be more diffused and the shear layers to be less distinct in comparison with the scenarios developed in the region between pin-rows 3–5.

With detached pin-fins of $C/d \leqslant 1$, the flow mechanisms in association with pin-wall junctions on the endwall are diminished but the vortex shading process as well as the enhanced turbulent mixing tripped by the protruding pin-fins still prevail over the mainstream. Instead of the horseshoe vortices developed on the endwall mounted with attached pin-fins, the accelerated flow through the gap between each pin-tip and the endwall modifies the boundary layer behaviors. Also the redistribution of flow rate through the gap at each tested *Re* with a pre-defined airflow rate considerably alters the *X*-wise velocity profiles that induces secondary vertical velocities heading toward the untouched endwall [33]. In this respect, the streamwise velocity within the detached pin-fin array is low and rather uniform, while the streamwise velocity above each pin-tip in the gap is much higher. Regions adjacent to the pin-tips form the intermediate layers with severe velocity gradients, resembling the conventional shear layer flows [33]. Extents of these accelerated shear layers emanated from the gaps between pin-tips and the endwall result in local heat transfer elevations as marked underneath each pin as shown in Fig. 2b and c. Such local HTE effects due to accelerated shear layers in the gaps above pin-tips are systematically faded when the C/d ratio increases from 1/4 to 2/4 and vanished as $C/d = 3/4$ (see Fig. 2b–d). However, it is persistently showed in Fig. 2b–d that two streamwise stripes with low *Nu* values of 2–3*d* bandwidths develop along the *X*-wise axes between $Y/D = 0.5$–1 and 1.5–2 on the endwall with detached pin-fins. This particular heat transfer phenomenon can be relevant with the flow interactions between the channel sidewalls and the accelerated shear layers emanating from the gapes above the pin-fins from the detached pins adjacent to two sidewalls. Further increases of C/d ratio widen such low *Nu* stripes and moderate the spatial *Nu* differences among these two axial stripes in the regions of $Y/D = 0.5$–1 and 1.5–2. Future works are worthwhile in order to clear the flow physics responsible for such systematic *Nu* variations along the streamwise axes between $Y/D = 0.5$–1 and 1.5–2 on the endwall with detached pin-fins. Justified by the pair of high *Nu* stripes with the bandwidth of about 1*d* alongside the edges of two sidewalls as seen in Fig. 2b–d, the corner vortices in the rectangular channels with detached pin-fins, which roll the cooler fluids toward the heated endwall along two sidewalls, are likely induced by the flow interactions between the pin-tip flow and the sidewall. Another worth noting observation is the weakened HTE effects offered by the wake shading and turbulent mixing over the endwall when the C/d ratio increases from 0 to 3/4. As illustrated previously, the two competing flow mechanisms, namely the increased downstream turbulent mixing due to wake shading from upstream pin-rows and the downstream thickened boundary layers, result in the low *Nu* entry region prior to the third pin-row as seen in Fig. 2a. Such entry regions with relatively low *Nu* values systematically expand further downstream as the C/d ratio increases by way of the sequential examination of Fig. 2a–d. This particular heat transfer result reflects the weakened streamwise increasing rate of turbulent mixing as the C/d ratio increases. As a result, the competition between the enhanced downstream turbulent mixing and the thickened boundary layers requires the longer developing length to grant for streamwise heat transfer elevations. The number of pin-row that initiates the high heat transfer performances thus systematically increases from the third pin-row with the attached pin-fins array ($C/d = 0$) to the 5th–10th pin-rows with the detached pin-fins of $C/d = 1/4$, 2/4 and 3/4 as seen in Fig. 2a–d. The expansion of entry region with low *Nu* values due to the increase of C/d ratio from 0 to 3/4 is the main attribute for the systematic reduction of the area-averaged Nusselt number over the untouched endwall of the detached pin-fin channel. The heat transfer characteristics demonstrated by Fig. 2 are followed by all the present test results in the *Re* range of 10,000–30,000.

The impacts of C/d ratio on local heat transfer performances form the reference conditions with attached pin-fins ($C/d = 0$) are highlighted by normalizing the local Nusselt numbers on the endwall with detached pin-fins (Nu^D) to those with attached pin-fins (Nu^A). Fig. 3 shows the distributions of Nu^D/Nu^A ratio on the endwalls with the detached pin-fins of (a) $C/d = 1/4$, (b) $C/d = 2/4$ and (c) $C/d = 3/4$ at $Re = 30{,}000$. Due to the lack of flow mechanisms triggered by pin-wall junctions, the larger degrees of abrupt entrance effect due to boundary layer developments generate the higher heat transfer rates at the flow entrance over the untouched endwalls with detached pin-fins. The accelerated flows emanating from the gaps above the detached pin-tips as well as the development of corner vortices along two sidewalls of the channels with detached pin-fins incur the local elevations of Nu^D/Nu^A ratios over the regions along two side edges of the detached pin-fin array adjacent to the channel sidewalls. But within the pin-fin array, the lack of pin-endwall junction effects in the channels with detached pin-fins considerably weakens the endwall HTE effect in the developing flow region. A sequential examination of Nu^D/Nu^A distributions as shown in Fig. 3a–c indicates the downstream expansion of low Nu^D/Nu^A regions. These regions with low Nu^D/Nu^A ratios correspond with the locations of low *Nu* values depicted in Fig. 2b–d. Such low *Nu* regions over the untouched endwall in the channels with detached pin-fins counter-pose the high *Nu* regions over the endwall with attached pin-fins. As a result, the lowest Nu^D/Nu^A ratios emerge in the first 2–5 rows of these detached pin-fin arrays.

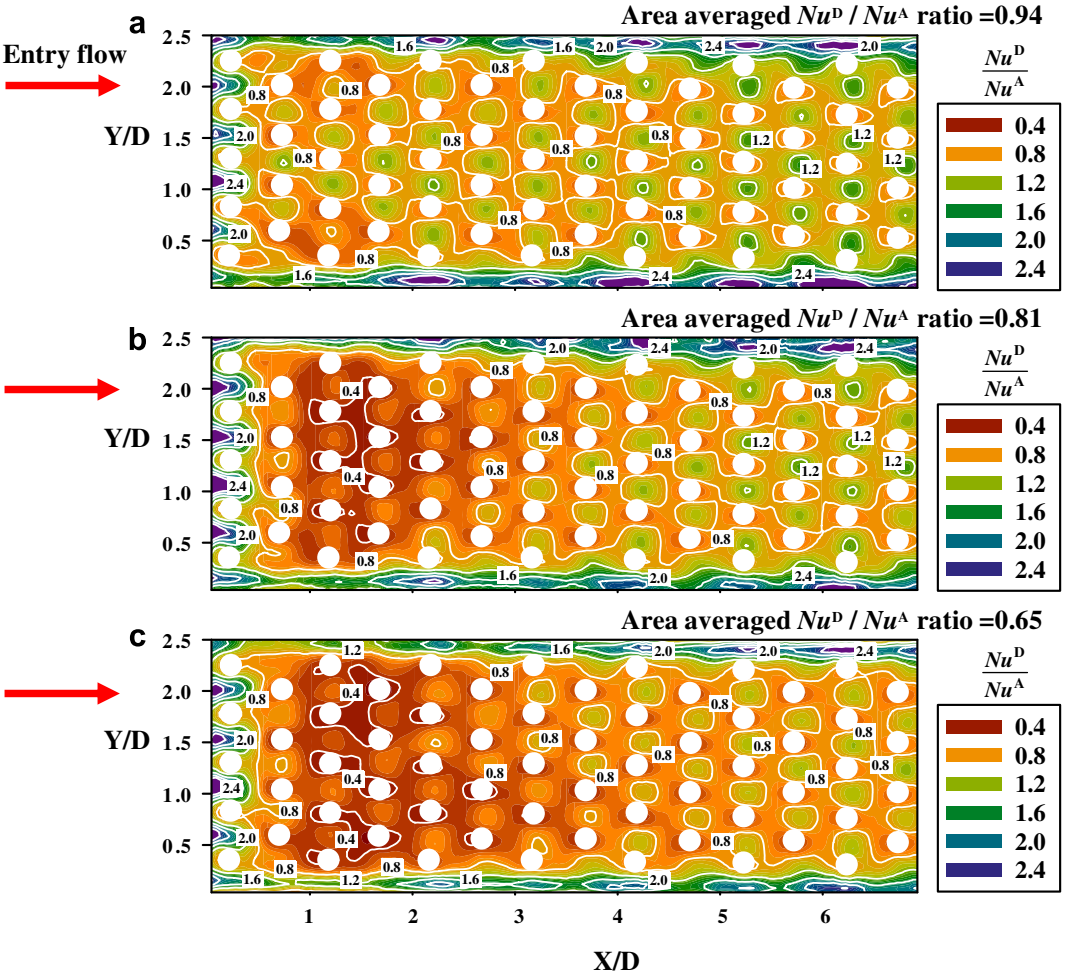

Fig. 3. Endwall distributions of Nu^D/Nu^A ratio for test channels with (a) attached pin-fins (b) detached pin-fins of C/d = 1/4, (c) detached pin-fins of C/d = 2/4 and (d) detached pin-fins of C/d = 3/4 at Re = 30,000.

Further downstream, local heat transfer elevations aside each pin start emerging even if the enhanced endwall heat transfer levels above each detached pin is not shown in Fig. 3a–c. These heat transfer characteristics highlighted by the distributions of Nu^D/Nu^A ratio over the untouched endwall are attributed from the modifications of local flow structures from the vortex dominant flow (attached pin-fins) to the conventional shear layer flow (detached pin-fins) by opening a small gap between pin and endwall. A considerable amount of locus where the ratios of Nu^D/Nu^A are above than unity emerges in the developed flow region over the endwalls with detached pin-fins as shown in Fig. 3. Therefore, the extension of developed flow region relative to the area occupied by the developing flow for such a detached pin-fin channel can assist the further elevation of area-averaged endwall Nu^D/Nu^A ratios. As the increase of C/d ratio from 1/4 to 3/4 extends the regions with low Nu^D values, the developing length required to generate the local heat transfer elevations from the counterparts of the attached pin-fin channel is increased. With Re = 30,000, the area averaged Nu^D/Nu^A ratios over the untouched endwalls with the detached pin-fins of C/d = 1/4, 2/4 and 3/4 are 0.94, 0.81 and 0.65 respectively.

Comparisons of X-wise Nu profiles collected from the pin-fin channels of C/d = 0, 1/4, 2/4 and 3/4 at various spanwise (Y/D) locations with Re = 30,000 are displayed in Fig. 4 where the corresponding X-wise location in the pin-fin array are marked underneath each plot of Fig. 4. The X-wise Nu profiles through the central region (Fig. 4a–c) and through the sidewall region (Fig. 4e–f) of the pin-fin array reflect different heat transfer results due to the different pin–pin and pin–sidewall interactions. In this respect, the comparative pairs are formulated as Fig. 4-a versus e, b versus f and c versus d. Without the influences from channel sidewall, the X-wise Nu profiles between each comparative pair of 4-a vs. 4-e, 4-b vs. 4-f or 4-c vs. 4-d will be very much alike.

Fig. 4a depicts the X-wise Nu profiles along the stagnation line of pin-fin array showing the impacts of pin–pin interactions within the pin-fin array. As compared in Fig. 4a, the channel with attached pin-fins shows the considerable Nu oscillations relative to those collected from the channels with detached pin-fins. For all the pin-fin channels compared in Fig. 4, local Nu values in the developing flow region increase in the streamwise direction. This distributing pattern is in contrast to that of typical ducted flow in which the heat transfer rates decrease in the developing flow region toward the developed level. But the developing lengths for such pin-fin channels vary with C/d ratio. In the channel with attached pin-fins (C/d = 0), the periodically repeated Nu variations are soon developed after the mainstream flow traverses three rows of pin-fins; while the "stable" Nu levels develop after the 5th, 9th and 10th pin-rows in the channels with detached pin-fins of C/d = 1/4, 2/4 and 3/4 respectively. The axial entry length systematically increases as the C/d ratio increases form 0 to 3/4. Oscillatory amplitudes in these X-wise Nu variations are systematically reduced as the C/d ratio increases form 0 to 3/4. It is interesting to note the

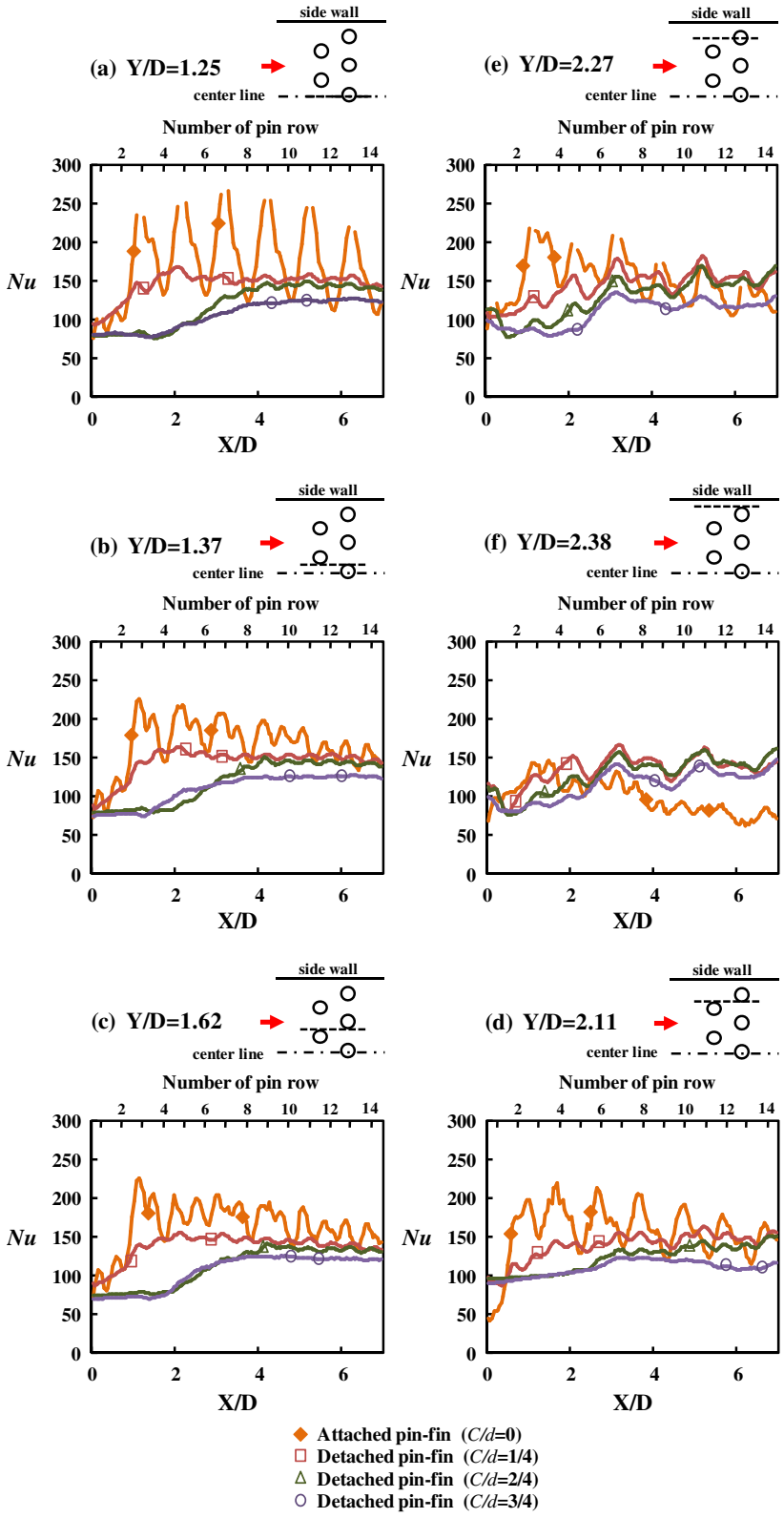

Fig. 4. *X*-wise *Nu* profiles at various *Y* locations for pin-fin channels with C/d = 0, 1/4, 2/4 and 3/4 at Re = 30,000.

high endwall *Nu* peaks atop these detached pin-fins. Such high endwall *Nu* peaks due to flow accelerations in the gaps above pin-tops are systematically moderated as C/d ratio increases and almost vanished with C/d = 3/4 as shown in Fig. 4a.

Fig. 4e depicts the *X*-wise *Nu* variations along another stagnation line of Y/D = 2.27 which are affected by the channel sidewall. As shown in Fig. 4e, the *Nu* oscillations in the channel with attached pin-fins are considerately moderated from the scenarios depicted in Fig. 4a; while such *Nu* oscillations in the channels with detached pin-fins are amplified from the counterparts showed by Fig. 4a. Comparing the heat transfer results collected in Fig. 4a and e, it is evident that the *Nu* levels with the attached pin-fins

are reduced due to the influences of channel sidewall. Although the influences of channel sidewall considerably impair the heat transfer levels in the channels with attached pin-fins and amplify the *Nu* oscillations in the channels with detached pin-fins along the stagnation line of the pin-row adjacent to the channel sidewall, the axial developing lengths in four tested channels seem to be unaffected by such sidewall effects. In particular, as compared in Fig. 4e, the *Nu* levels in the channels with detached pin-fins of $C/d = 1/4$ and 2/4 turn to be higher than those in the channel with attached pin-fins over the developed flow regions. In this respect, such different sidewall effects between the channels with attached and detached pin-fins suggest the different modes of sidewall interactions with the vortex mechanisms induced by the pin-endwall junction and the accelerated flows emanating from the pin-tips.

The *X*-wise *Nu* variations along two side edges of the streamwise pin-rows through the central region of the pin-fin array in each test channel, which are separately showed in Fig. 4b and c, are almost identical due to the lack of channel sidewall effects. Results collected in Fig. 4b and c consistently show that the amplitudes of *Nu* oscillations along two side edges of the attached pin-fins are considerably moderated from the scenarios depicted in Fig. 4a; while the magnitudes of *Nu* peaks along two side edges of the detached pin-fins with $C/d = 1/4$ and 2/4 almost remain unchanged from the results detected along the stagnation line of the central pin-row as shown in Fig. 4a. This particular finding demonstrates the different flow physics that dominate the heat transfer performances around each attached and detached pin-fins. Referring to the flow structures described in the introduction section for the channel with attached pin-fins, the vortex complex tripped by the pin-endwall junction generates considerably circumferential *Nu* variations around each pin-fin. With the small gaps above the detached pins, the boundary layer type accelerated flows develop over these detached pin-tips, which are rather uniformly distributed over the pin-tips and give rise to the negligible differences between the *Nu* profiles along the stagnation line (see Fig. 4a) and along two side edges (see Fig. 4b and c) of the detached pin-fins. In the central region of the pin-fin array with detached pin-fins of $C/d = 1/4$, 2/4 and 3/4, the small differences in the *X*-wise *Nu* profiles along the stagnation line as shown in Fig. 4a and along two side edges of the streamwise pin-row as shown in Fig. 4b and c reflect the impacts of uniform accelerated flows above each pin-tip over the endwall that generate the very moderate circumferential endwall *Nu* variations over each detached pin-fin. But the channel sidewall still provides considerable impacts on the *X*-wise *Nu* variations along two side edges of the *X*-wise pin-row after the cross examinations of Fig. 4b versus f and c versus d.

By way of comparing the *X*-wise *Nu* profiles along the stagnation line and two side edges of the *X*-wise pin-row adjacent to the channel sidewall for both attached and detached pin-fins as shown in Fig. 4d–f, the considerably *Nu* differences between those along the stagnation line and along two side edges of this *X*-wise pin-row demonstrates the generation of circumferential *Nu* variations on the endwall over each attached or detached pin-fin region due to the sidewall effects. By comparing the *Nu* profiles collected in Fig. 4c and d, the levels and distributing patterns of *X*-wise *Nu* variations along the same side edges of two different *X*-wise pin-rows at $Y/D = 1.62$ (central region) and $Y/D = 2.11$ (sidewall region) are similar in the channels of $C/d = 0$ and 1/4 but are different in the channels of $C/d = 2/4$ and 3/4. The *Nu* levels in the developing flow regions of the two test channels of $C/d = 2/4$ and 3/4 depicted in Fig. 4d are getting higher than those counterparts showed in Fig. 4c as a result of channel sidewall effects. Further shift of the *X*-wise profile toward the channel sidewall from $Y/D = 2.11$ (Fig. 4d) to the spanwise location of $Y/D = 2.38$ (Fig. 4f) amplifies the *X*-wise *Nu* variations from those within the central region of pin-fin array. By comparing the *X*-wise *Nu* profiles collected in Fig. 4b and f for the attached pin-fin channel ($C/d = 0$), it is noticed that the *Nu* levels and the *Nu* oscillations along this side edge of the *X*-wise pin-row at the location of $Y/D = 2.38$ are considerably suppressed. The stagnant pressure field built along the sidewall corner of the test channel with attached pin-fins is likely to suppress the vortex motion and turbulent activities which lead to the moderate pin-wise *Nu* oscillations accompanying by the lower heat transfer rates. On the contrast, the channel sidewall effects augment the *Nu* oscillations along the side edge of the *X*-wise pin-row at the location of $Y/D = 2.38$ for the detached pin-fins of $C/d = 1/4$, 2/4 and 3/4 from their counterparts displayed in Fig. 4b for the central regions of pin-fin arrays. As compared in Fig. 4f, the *Nu* levels in the developing flow regions of the four pin-fin channels with $C/d = 0$, 1/4, 2/4 and 3/4 are compatible; while the *Nu* levels in the developed flow regions of the detached pin-fin channels with $C/d = 1/4$, 2/4 and 3/4 are considerably higher than those in the channel with attached pin-fins ($C/d = 0$). Giving the two different types of heat transfer variations between the attached and detached pin-fin channels in responding to the channel sidewall effects, two different types of corner-flow structures are generated along two sidewalls in the channels with attached and detached pin-fins. The detailed flow measurements are worthwhile in order to clear the flow physics responsible for such heat transfer variations.

Fig. 5 shows the *Y*-wise *Nu* profiles across the leading edge (a), central section (b) and trailing edge (c) of the 10th pin-row and (d) the middle section between the 10th and 11th pin-rows at $Re = 30{,}000$. While the similar levels and distributing patterns of *Y*-wise *Nu* profiles in the developed flow regions of three detached pin-fin channels are observed at the four X/D locations showed in Fig. 5a–d, the complex vortex mechanisms developed in the channel with attached pin-fins result in different *Y*-wise *Nu* patterns and *Nu* levels along the leading edge, central section, trailing edge of a pin-row and along the middle section between two adjacent pin-rows. The most considerable *Y*-wise *Nu* variations develop along the leading edge of the 10th pin-row for the channel with attached pin-fins. With the attached pin-fins, the *Y*-wise *Nu* values along the trailing edge of the 10th pin-row showed in Fig. 5c are higher than those counterparts across the central sections of the 10th pin-row as indicated in Fig. 5b. But across the middle section between two adjacent pin-rows in the developed flow region of each test channel with attached or detached pin-fins, the *Y*-wise *Nu* oscillations tend to be diminished. The magnitudes of the spanwisely averaged *Nu* values across the leading edges, central sections, trailing edges of the pin-row or across the middle section between two adjacent pin-rows in the developed flow regions consistently follow the order of $C/d = 0$, 1/4, 2/4 and 3/4. However, in the regions near two channel sidewalls, the local *Nu* values follow the order of $C/d = 1/4$, 2/4, 3/4 and 0. As illustrated previously, such low heat transfer performances aside two channel sidewalls in the developed flow region with attached pin-fins are mainly attributed from the suppressed vortex activities triggered by the pin-junction effects over the endwall. Above all, the spatial endwall *Nu* variations in the channels with detached pin-fins of $C/d = 1/4$, 2/4 and 3/4 are considerably less than those with the attached pin-fins. The less degree of spatial endwall *Nu* variations in each test channel with the detached pin-fins serves as an additional merit for industrial applications due to the less wall temperature gradients induced.

3.2. Heat transfer correlation

A set of heat transfer correlations that evaluates the area averaged endwall Nusselt number level for the present pin-fin configuration with $P_x/d = P_y/d = 2$ and $H/d = 2.5$ is derived using *Re* and C/d as the controlling parameters. The area averaged heat transfer

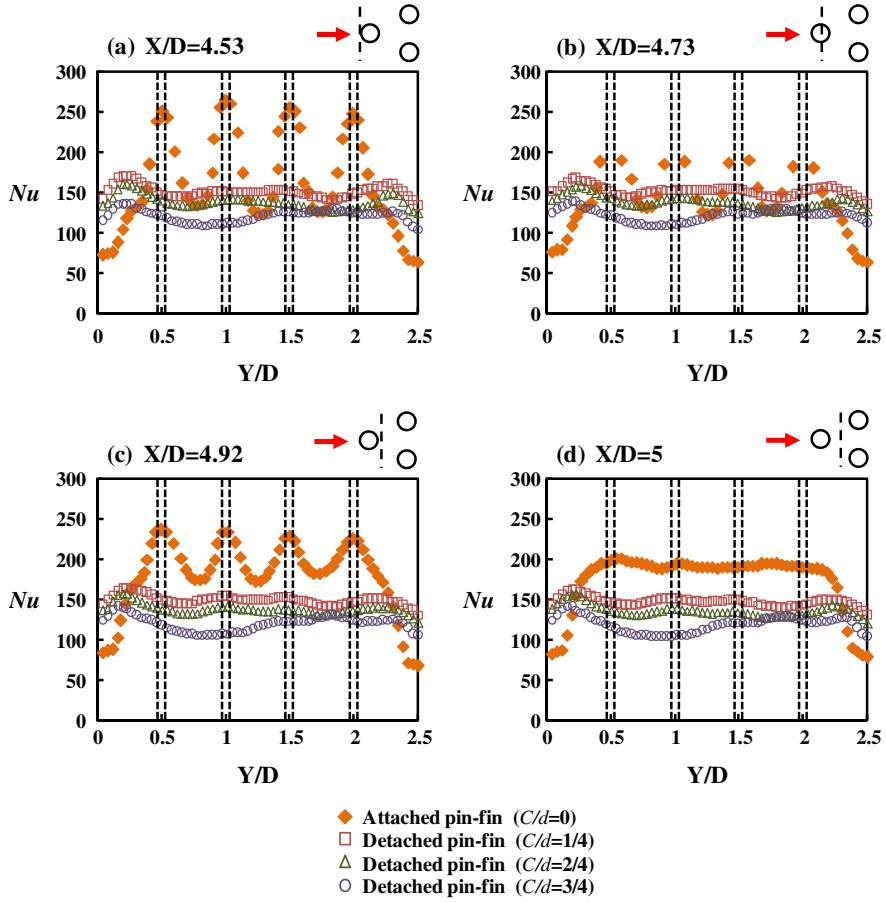

Fig. 5. *Y*-wise *Nu* profiles at various *X* locations for pin-fin channels with C/d = 0, 1/4, 2/4 and 3/4 at Re = 30,000.

level at each tested Re is obtained by averaging the Nusselt numbers over the endwall as $\overline{Nu}$. The regressive analysis aimed at deriving the $\overline{Nu}$ correlation for four sets of pin-fin channels with C/d = 0, 1/4, 2/4 or 3/4 is initiated by examining the varying manners of $\overline{Nu}$ against Re for four tested pin-fin channels as shown in Fig. 6. For the purpose of validation, Fig. 6 also collects the endwall heat transfer data reported in [27,34,35] for the channels with attached pin-fins which share the similar test configurations with the present study. As compared in Fig. 6, the comparison of $\overline{Nu}$ derived by Lyall et al. [35] with present $\overline{Nu}$ at Re = 30,000 yields 7% lower values of present Nu than those reported by Lyall et al. [35]; whereas the comparison of present $\overline{Nu}$ with $\overline{Nu}$ derived by Chyu et al. [34] at Re = 18000 results in 17% lower values of present

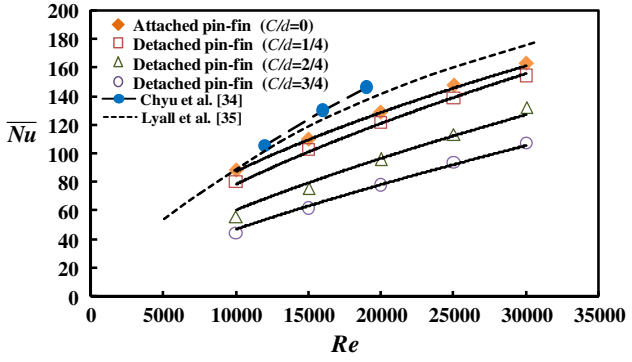

Fig. 6. Comparison of endwall area-averaged *Nu* values for the pin-fin channels with C/d = 0, 1/4, 2/4 and 3/4.

$\overline{Nu}$. These discrepancies can be attributed to differences in channel aspect ratio, pin pitch ratio, experimental setup and boundary conditions. Giving the satisfactory comparisons between present $\overline{Nu}$ data with the results reported by other research groups for the channels with attached pin-fins, the subsequent data analysis aimed at revealing the impacts of C/d ratio on $\overline{Nu}$ is performed. As shown in Fig. 6, the $\overline{Nu}$ levels in these four pin-fin channels at each Re tested systematically decrease as the C/d ratio increases from 0 to 3/4. But the reductions in $\overline{Nu}$ from the reference levels of attached pin-fin channel are only about 7% for the detached pin-fin channel with C/d = 1/4. As displayed in Fig. 6 for each C/d controlled data series, the $\overline{Nu}$ value increases with the increase of Re that follows a general trend specified in Eq. (3) which automatically satisfies the limiting condition of diminished forced convective capability ($\overline{Nu} \to 0$) as $Re \to 0$.

$$\overline{Nu} = A\{C/d\} \times Re^{B\{C/d\}} \tag{3}$$

With the present pin-fin configurations, the coefficient A and exponent B in Eq. (3) are functions of C/d. Table 1 summarizes the coefficients A and exponents B derived for four test channels with C/d = 0, 1/4, 2/4 and 3/4.

Table 1
Coefficient A and exponent B for test channels of C/d = 0, 1/4, 2/4 and 3/4

C/d ratio of pin-fins	A	B	Correlation factor (r^2)
0 (attached pin-fins)	0.507	0.6	0.999
1/4 (detached pin-fins)	0.261	0.62	0.998
2/4 (detached pin-fins)	0.115	0.68	0.983
3/4 (detached pin-fins)	0.051	0.74	0.995

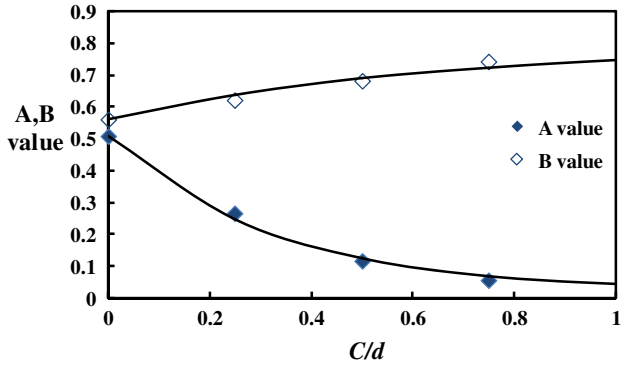

Fig. 7. Variations of A, B values with C/d ratio.

The systematic decrease of A coefficient accompanying with the systematic increase of B exponent as C/d ratio increases is clearly indicated in Table 1. Such trends of variation for A and B values against C/d ratio are showed in Fig. 7 that reflect the enhanced impacts of forced convection on heat transfer from the scenarios dominated by the vortex complex in the channel with attached pin-fins as the C/d ratio increases from 0 to 3/4. Nevertheless, as the C/d ratio increases to the limiting condition that features the so-called zero pin height ($C/d > 2.5$ for present cases), the heat transfer results shall recast the conditions of forced convection in the rectangular channel with smooth walls. The existence of limiting condition equivalent to the forced convective flow in the smooth-walled channel predefines the functional structure of A and B values as the exponential complex function which are respectively derived as Eqs. (4) and (5).

$$A = 0.02 + 0.487e^{-3.13C/d} \quad (4)$$

$$B = 0.8 - 0.241e^{-1.52C/d} \quad (5)$$

It is interesting to note the asymptotic A, B values evaluated from Eqs. (4) and (5) which show the close agreements with the coefficients in the $\overline{Nu}$ correlations for smooth-walled channels. The maximum discrepancies between the correlated results from Eq. (3) and the experimental measurements are controlled within the range of ±14% for the entire $\overline{Nu}$ data generated.

3.2.1. Pressure drop measurements and correlation

Fig. 8 depicts the variations of Fanning friction factors (f) against Re for four test channels with C/d = 0, 1/4, 2/4 and 3/4. The present f values are calculated from the pressure drops across the entire length of test channel (L) with the characteristic length selected as the channel hydraulic diameter (D). The f correlation reported by Zukauskas et al. [36] for the attached pin-fin channel with the similar pin-fin and channel geometries is also plotted in Fig. 8a to validate the present f measurements. As compared in Fig. 8a, favorable agreements between the present f data and the correlation of Zukauskas et al. [36] for the channels with attached pin-fins are demonstrated. For each test channel with attached or detached pin-fins, the Fanning friction factors increase with the increase of Re. This f versus Re trend is closely relevant to the pin height-to-diameter (H/d) ratio that agrees with the correlation reported in [36]. But in the channels with attached pin-fins of $H/d < 1.5$ [27,34], the f values generally decrease with the increase of Re. A further increase of H/d ratio enlarges the friction and pressure drags inside the pin-fin channels that can lead to the increased f values as Re increases for the pin-fin channels with $H/d \geqslant 2.5$ such as the pin-fin geometries examined by Zukauskas et al. [36] and present study. Nevertheless, the significant reductions of f values from the reference conditions defined by the attached pin-fin channel are observed for all the detached pin-fin channels as

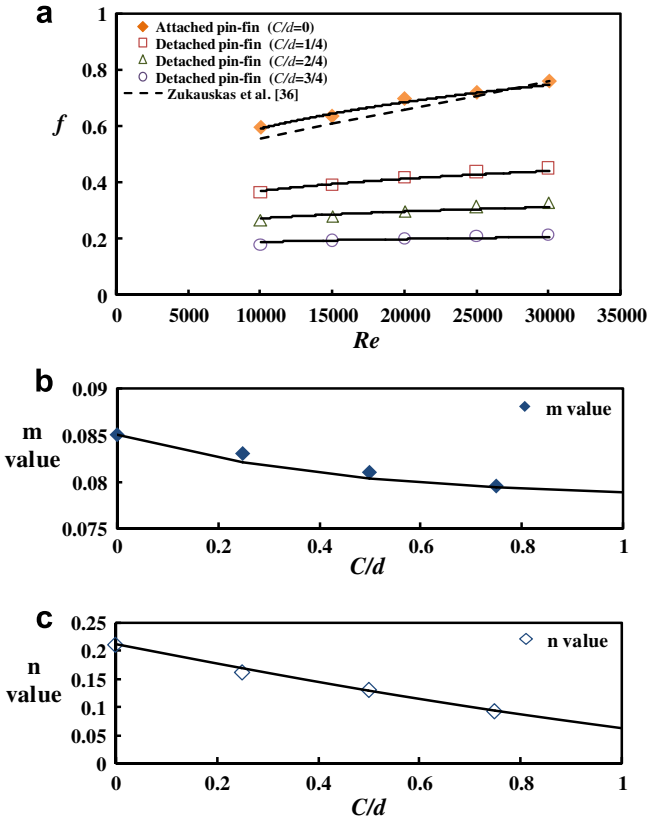

Fig. 8. Variations of (a) f factor with Re and (b) m value (c) n value with C/d ratio.

shown in Fig. 8a. The f values in the detached pin-fin channels with C/d = 1/4, 2/4 and 3/4 fall considerably to the levels about 0.6, 0.43 and 0.29 times of the Fanning friction factors in the attached pin-fin channel. In this respect, the absence of pin-junction mechanisms over one endwall in the channel with detached pin-fins of C/d = 1/4 has considerably reduced the pressure drop penalties with only minor reductions in the endwall $\overline{Nu}$ values. It is noticed that, with the additional convective area projected by the detached pin-fins on the endwall, the total convective area available for the present channel with detached pin-fins of C/d = 1/4 is 1.1 times of the pin-area in the attached pin-fin channel. Such thermal fluid characteristics offer considerable advantages for the cooling applications with only one heated endwall.

Justified by the data trends depicted in Fig. 8a, the f value for each tested pin-fin channel is the function of C/d and Re. In the range of $10{,}000 \leqslant Re \leqslant 30{,}000$, Fanning frictions factors in the present test channels with attached and detached pin-fins are respectively correlated as:

$$f = m\{C/d\} \times Re^{n\{C/d\}} \quad (6)$$

Coefficients m and exponents n in Eq. (6) are summarized in Table 2 four test channels with C/d = 0, 1/4, 2/4 and 3/4.

The varying manners of m, n values against C/d ratio as depicted in Table 2 echo the data trends of A, B coefficients revealed in Figs. 8b and c that approach the asymptotic smooth-walled channel conditions. With the consideration of featuring the so-called zero pin-height scenarios as the C/d ratio reaches the limiting conditions, the m, n values are derived as Eqs. (4) and (5) respectively.

$$m = 0.078 + 0.007e^{-2.16C/d} \quad (7)$$

$$n = -0.397 + 0.608e^{-0.298C/d} \quad (8)$$

Correlations (7) and (8) infer that the further increase of C/d ratio can lead to the negative n exponent with coefficient m reduced.

Table 2
Coefficient m and exponent n for test channels of C/d = 0, 1/4, 2/4 and 3/4

C/d ratio of pin-fins	m	n	Correlation factor (r^2)
0 (attached pin-fins)	0.085	0.211	0.982
1/4 (detached pin-fins)	0.083	0.16	0.985
2/4 (detached pin-fins)	0.081	0.138	0.969
3/4 (detached pin-fins)	0.08	0.089	0.956

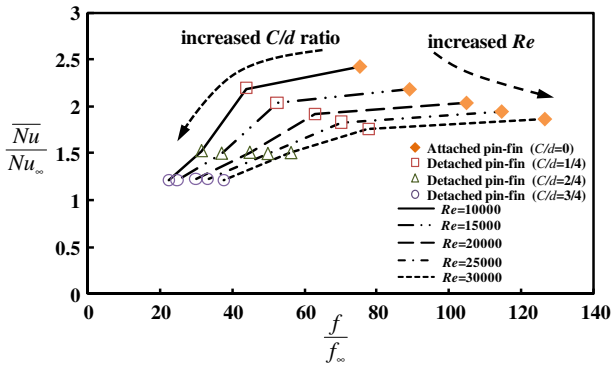

Fig. 9. Variations of $\overline{Nu}/Nu_\infty$ with f/f_∞ for the pin-fin channels with C/d = 0, 1/4, 2/4 and 3/4 at Re = 10,000, 15,000, 20,000, 25,000 and 30,000

Maximum discrepancies between the correlated f values evaluated from Eq. (6) and the experimental data are less than ±11% for the entire f data generated.

Augmentations of $\overline{Nu}$ and f values from the smooth-walled references for the pin-fin channels with C/d = 0, 1/4, 2/4 and 3/4 are indexed by the ratios of $\overline{Nu}/Nu_\infty$ and f/f_∞ respectively. In view of the C/d impacts on $\overline{Nu}$ and f values as described by Figs. 6 and 8 respectively, the moderation of endwall HTE effect is accompanying with the reduction of pressure drop penalty as C/d ratio increases from 0 to 3/4. Such comprises between the HTE effect and the pressure drop penalty due to the variations of C/d ratio are illustrated by plotting $\overline{Nu}/Nu_\infty$ ratio against f/f_∞ ratio as shown in Fig. 9. At each tested Re as seen in Fig. 9, the increase of C/d ratio drives the data points obtained with C/d = 0, 1/4, 2/4 and 3/4 toward the asymptotic smooth-walled condition of $\overline{Nu}/Nu_\infty = f/f_\infty = 1$. Although all the data series connecting by the four data points collected from C/d = 0, 1/4, 2/4 and 3/4 follow a similar trend, the increase of Re systematically moderates such varying trend with a tendency to flatten the data trend constructed by the data points obtained with various C/d ratios as $Re \to \infty$. In other words, the increase of C/d ratio toward the smooth-walled condition ($C/d \to \infty$) at a finite Re value incurs the diminished HTE effect ($\overline{Nu}/Nu_\infty = 1$) with the vanished increase in pressure drop ($f/f_\infty = 1$). But as $Re \to \infty$ with a finite C/d ratio, the $\overline{Nu}/Nu_\infty$ ratio approaches unity with the f/f_∞ ratio approaches ∞. Therefore the trade-off between HTE effects and pressure drop penalties is in favor of the test condition with Re = 10,000 rather than the condition of Re = 30,000 for the present test channel with attached or detached pin-fins. As indicated in Fig. 9, the $\overline{Nu}/Nu_\infty$ (f/f_∞) ratios for the present tested pin-fin channels fall in the ranges of 1.86–2.43 (75.2–126.6) with C/d = 0, 1.75–2.22 (43.9–77.5) with C/d = 1/4, 1.49–1.53 (31.4–56.1) with C/d = 2/4 and 1.21–1.23 (22.4–37.7) with C/d = 3/4.

3.3. Thermal performance factor

The assessment of thermal performances for the pin-fin test channels with different C/d ratios is performed by comparing their η factors based on the same pumping power consumption. Fig. 10

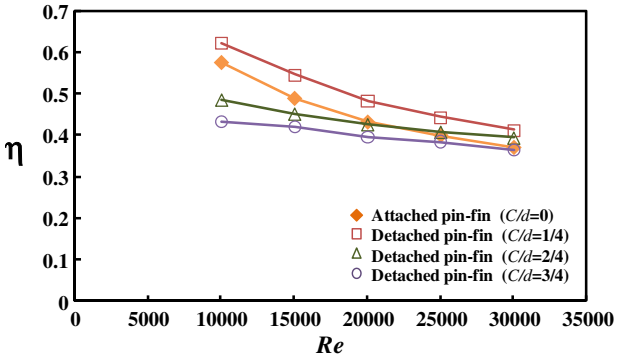

Fig. 10. Variations of thermal performance factor (η) with Re for the pin-fin channels with C/d = 0, 1/4, 2/4 and 3/4.

shows the variations of η factor against Re at each C/d ratio tested. As shown in Fig. 10 for each C/d controlled data series, η factors decrease with the increase of Re. This particular η versus Re trend is due to the decrease of $\overline{Nu}/Nu_\infty$ ratio and the increase of f/f_∞ ratio as Re increases. In the Re range of 10,000–30,000, the highest η factors consistently develop in the channel with detached pin-fins of C/d = 1/4. With $Re \leqslant$ 20,000, η factors generally follow the order of $\eta_{C/d=1/4} > \eta_{C/d=0} > \eta_{C/d=2/4} > \eta_{C/d=3/4}$ as compared Fig. 10. But with Re = 25,000 and 30,000, the η factors for the detached pin-fin of C/d = 2/4 are getting higher than those in the channel with attached pin-fins. Judging by the occasional demands for applications, the selection of detached or attached pin-fins as the passive HTE measure offers different characteristics either with the larger HTE effects or with the higher η factors. In accordance with the thermal fluid characteristics depicted in Fig. 9, the CPU cooling unit that takes the pressure drop as a serious design consideration and often operates at the low Re (Re < 10,000) with one heated wall is particularly suitable to adopt the detached pin-fins of small C/d ratio such as C/d = 1/4 as its HTE measure.

4. Conclusions

This experimental study performs measurements of detailed endwall heat transfer distributions and entry-to-exit pressure drops for four rectangular channels with attached pin-fins (C/d = 0) and detached pin-fins of C/d = 1/4, 2/4 and 3/4. The major contribution of this work is the first time investigation of endwall heat transfer and pressure drop performances in the pin-fin channel with the C/d ratios less than unity, which discovers the considerable decreases of channel pressure drops with moderate heat transfer reductions by opening the small gaps between the pin-tips and the channel endwall. The detailed endwall Nu data along with the Fanning friction factors (f) for these pin-fin channels with Re range of 10,000 $\leqslant Re \leqslant$ 30,000 are acquired and the empirical correlations for area-averaged Nusselt number ($\overline{Nu}$) and f factor generated. Due to the differences in flow structures over the channel endwall between attached and detached pin-fins, the $\overline{Nu}/Nu_\infty$ (f/f_∞) ratios for these four pin-fin channels fall in the ranges of 1.86–2.43 (75.2–126.6) with C/d = 0, 1.75–2.22 (43.9–77.5) with C/d = 1/4, 1.49–1.53 (31.4–56.1) with C/d = 2/4 and 1.21–1.23 (22.4–37.7) with C/d = 3/4. f values in the detached pin-fin channels with C/d = 1/4, 2/4 and 3/4 fall considerably to the levels about 0.6, 0.43 and 0.29 times of the Fanning friction factors in the attached pin-fin channel. With detached pin-fins of C/d = 1/4, the reductions in $\overline{Nu}$ values form the attached pin-fin references are only about 7%, while the f values in the detached pin-fin channels with C/d = 1/4 fall considerably to the levels about 0.41 times of the Fanning friction factors in the attached pin-fin channel. Within the present Re range tested, the highest η factors constantly develop in

the channel with detached pin-fins of $C/d = 1/4$. With $Re \leqslant 20{,}000$, the η factors for four tested channels follow the order of $\eta_{C/d=1/4} > \eta_{C/d=0} > \eta_{C/d=2/4} > \eta_{C/d=3/4}$ but such order between $\eta_{C/d=0}$ and $\eta_{C/d=2/4}$ are reverted at $Re = 25{,}000$ and 30,000. The hydraulic gain in reducing the channel pressure drops by introducing small gaps ($C/d < 1$) above the detached pin-fins accompanying with the moderate heat transfer reductions has made the HTE measure of detached pin-fin channel suitable for the applications with only one heated wall in which the pressure drop reductions play the important role for design activities such as the CPU cooling unit.

References

[1] E.M. Sparrow, J.W. Ramsey, Heat transfer and pressure drop for a staggered wall-attached array of cylinders with tip clearance, Int. J. Heat Mass Transfer 21 (1978) 1369–1377.

[2] E.M. Sparrow, J.W. Ramsey, C.A.C. Altemani, Experiments on in-line pin fin arrays and performance comparisons with staggered array, ASME J. Heat Transfer 102 (1980) 44–50.

[3] D.E. Metzger, R.A. Berry, J.P. Bronson, Developing heat transfer in rectangular ducts with staggered arrays of short pin fins, ASME J. Heat Transfer 104 (1982) 700–706.

[4] G.J. Van Fossen, Heat-transfer coefficients for staggered arrays of short pin-fins, ASME J. Eng. Power 104 (1982) 268–274.

[5] R.J. Simoneau, G.J. Van Fossen, Effects of location in an array on heat transfer to a short cylinder in cross flow, ASME J. Heat Transfer 106 (1984) 42–48.

[6] D.E. Mezger, C.D. Fan, S.W. Haley, Effects of pin shape and array orientation on heat transfer and pressure loss in pin arrays, ASME J. Eng. Gas Turbines Power 106 (1984) 252–257.

[7] J. Armstrong, D. Winstanley, A review of staggered array pin fin heat transfer for turbine cooling applications, ASME J. Turbomach. 110 (1988) 94–103.

[8] M.K. Chyu, Heat transfer and pressure drop for short pin-fin arrays with pin-endwall fillet, ASME J. Heat Transfer 112 (1990) 926–932.

[9] E.M. Sparrow, V.B. Grannis, Pressure drop characteristics of heat exchangers consisting of arrays of diamond-shaped pin fins, Int. J. Heat Mass Transfer 34 (1991) 589–600.

[10] M.K. Chyu, R.J. Goldstein, Influence of cylindrical elements on local mass transfer from a flat plate, Int. J. Heat Mass Transfer 34 (1991) 2175–2186.

[11] V.B. Grannis, E.M. Sparrow, Numerical simulation of fluid flow through an array of diamond-shaped pin fins, Numer. Heat Transfer (Part A) 19 (1991) 381–403.

[12] B.A. Jubran, M.A. Hamdan, R.M. Abdualh, Enhanced heat transfer, missing pin and optimization for cylindrical pin fin arrays, ASME J. Heat Transfer 115 (1993) 576–583.

[13] M.K. Chyu, V. Natarajan, Effect of flow angle-of-attach on the local heat/mass transfer distributions from a wall-mounted cube, ASME J. Heat Transfer 116 (1994) 552–560.

[14] R.F. Babus'Haq, K. Akintude, S.D. Probert, Thermal performance of pin fin assembly, Int. J. Heat Fluid Flow 16 (1995) 50–55.

[15] M.K. Chyu, V. Natarajan, Heat transfer on the base surface of three-dimensional protruding elements, Int. J. Heat Mass Transfer 39 (1996) 2925–2935.

[16] M.K. Chyu, Y.C. Hsing, V. Natarajan, Convective heat transfer of cubic fin arrays in a narrow channel, ASME J. Turbomach. 120 (1998) 362–367.

[17] Q. Li, Z. Chen, U. Flechtner, H.-J. Warnecke, Heat transfer and pressure drop characteristics in rectangular channels with elliptic pin fins, Int. J. Heat Fluid Flow 19 (1998) 245–250.

[18] M.K. Chyu, Y.C. Hsing, T.I.-P. Shih, V. Natarajan, Heat transfer contributions of pins and endwall in pin-fin arrays: effects of thermal boundary condition modeling, ASME J. Turbomach. 121 (1999) 257–263.

[19] G. Tanda, Heat transfer and pressure drop in a rectangular channel with diamond-shaped elements, Int. J. Heat Mass Transfer 44 (2001) 3529–3541.

[20] O.N. Şara, Performance analysis of rectangular ducts with staggered square pin fins, Energy Convers. Manage. 44 (2003) 1787–1803.

[21] S.Y. Won, G.I. Mahmood, P.M. Ligrain, Spatially-resolved heat transfer and flow structure in a rectangular channel with pin fins, Int. J. Heat Mass Transfer 47 (2004) 1731–1743.

[22] D. Kim, S.J. Kim, A. Ortega, Compact modeling of fluid flow and heat transfer in pin fin heat sinks, ASME J. Electron. Packaging 126 (2004) 342–350.

[23] N. Sahiti, F. Durst, A. Dewan, Heat transfer enhancement by pin elements, Int. J. Heat Mass Transfer 48 (2005) 4738–4747.

[24] M.B. Dogruoz, M. Urdaneta, A. Ortega, Experiments and modeling of the hydraulic resistance and heat transfer of in-line square pin fin heat sink with top by-pass flow, Int. J. Heat Mass Transfer 48 (2005) 5058–5071.

[25] N. Sahiti, A. Lemouedda, D. Stojkovic, F. Durst, E. Franz, Performance comparison of pin fin in-duct flow arrays with various pin cross-sections, Appl. Therm. Eng. 26 (2006) 1176–1192.

[26] N. Sahiti, F. Durst, P. Geremia, Selection and optimization of pin cross-sections for electronics cooling, Appl. Therm. Eng. 27 (2007) 111–119.

[27] M.K. Chyu, E.O. Oluyede, H.-K. Moon, Heat transfer on convective surfaces with pin-fins mounted in inclined angles, GT2007-28138, ASME Turbo Expo (2007) May 14–17, Montreal, Canada.

[28] T.-M. Liou, M.-Y. Chen, Y.-M. Wang, Heat transfer, fluid flow and pressure measurements inside a rotating two-pass duct with detached 90-deg ribs, ASME J. Turbomach. 125 (2003) 565–574.

[29] S.W. Chang, T.-M. Liou, W.-J. Juan, Influence of channel height on heat transfer augmentation in rectangular channels with two opposite rib-roughened walls, Int. J. Heat Mass Transfer 48 (2005) 2806–2813.

[30] F.W. Dittus, L.M.K. Boelter, University of California, Berkeley, CA, Pub. in Engng. 2 (1930) 443.

[31] Eitorial Board of ASME Journal of Heat Transfer, Journal of heat transfer policy on reporting uncertainties in experimental measurements and results, ASME J. Heat Transfer 115 (1993) 5–6.

[32] A.K. Saha, S. Acharya, Parametric study of unsteady flow and heat transfer in a pin-fin heat exchanger, Int. J. Heat Mass Transfer 46 (2003) 3815–3830.

[33] B. Avisar, L. Shemer, A. Kribus, Measurements of velocity fields in finite cylinder arrays with and without tip clearance, Int. J. Exp. Therm. Fluid Sci. 24 (2001) 157–167.

[34] M.K. Chyu, C.H. Yen, S. Siw, Comparison of heat transfer from staggered pin fin arrays with circular, cubic and diamond shaped element, GT2007-28306, ASME Turbo Expo (2007) May 14–17, Montreal, Canada.

[35] M.E. Lyall, A.A. Thrift, Heat transfer from low aspect ratio pin fins, GT2007-27431, ASME Turbo Expo (2007) May 14–17, Montreal, Canada.

[36] A. Zukauskas, R. Ulinskas, Efficiency parameters for heat transfer in tube banks, Heat Transfer Eng. 6 (1985) 19–25.